ACS APPLIED MATERIALS & INTERFACES
Research Article
www.acsami.org

# Carbon Encapsulated Tin Oxide Nanocomposites: An Efficient Anode for High Performance Sodium-Ion Batteries

Ramchandra S. Kalubarme, Jae-Young Lee, and Chan-Jin Park*

Department of Materials Science and Engineering, Chonnam National University, 77 Yongbongro, Bukgu, Gwangju 500-757, South Korea

S Supporting Information

**ABSTRACT:** The major obstacle in realizing sodium (Na)-ion batteries (NIBs) is the absence of suitable negative electrodes. This is because graphite, a commercially well known anode material for lithium-ion batteries, cannot be utilized as an insertion host for Na ions due to its large ionic size. In this study, a simple and cost-effective hydrothermal method to prepare carbon coated tin oxide ($SnO_2$) nanostructures as an efficient anode material for NIBs was reported as a function of the solvent used. A single phase $SnO_2$ resulted for the ethanol solvent, while a blend of SnO and $SnO_2$ resulted for the DI water and ethylene glycol solvents. The elemental mapping in the transmission electron microscopy confirmed the presence of carbon coating on the $SnO_2$ nanoparticles. In cell tests, the anodes of carbon coated $SnO_2$ prepared in ethanol solvent exhibited stable cycling performance and attained a capacity of about 514 mAh $g^{-1}$ on the first charge. With the help of the conductive carbon coating, the $SnO_2$ delivers more capacity at high rates: 304 mAh $g^{-1}$ at the 1 C rate, 213 mAh $g^{-1}$ at the 2 C rate and 133 mAh $g^{-1}$ at the 5 C rate. The excellent cyclability and high rate capability are the result of the formation of a mixed conducting network and uniform carbon coating on the $SnO_2$ nanoparticles.

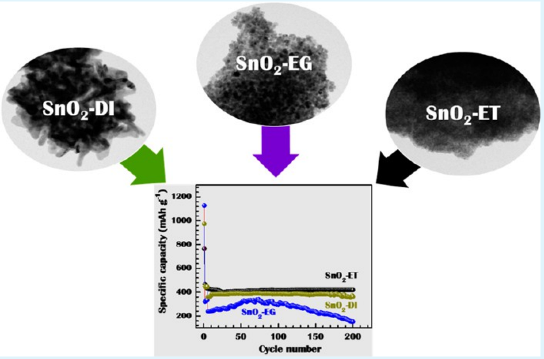

**KEYWORDS:** *sodium-ion battery, tin oxide/carbon composite, anode material, hydrothermal synthesis, conversion reaction, sodiation/desodiation*

## INTRODUCTION

Lithium-ion batteries (LIBs) have been considered as next-generation energy-storage and conversion devices, and have been widely used in portable electronic devices, electrical vehicles, and hybrid electrical vehicles, etc.[1] Particularly, they have become indispensable energy storage devices for intermittent energy conversions, such as in solar cells and for wind power. However, the low abundance and uneven distribution of lithium resources show the potential difficulties of the long-term and large-scale applications of lithium-ion batteries in terms of their availability and cost. Hence, the development of new types of batteries, such as sodium-ion and magnesium-ion batteries, is essential. Among them, Na-ion batteries (NIBs) possess electrochemical working principles that are similar to LIBs. In addition, sodium is inexpensive and abundant.[2] Sodium is the sixth richest element on earth. Therefore, NIBs could substitute LIBs in applications such as smart grids and large-scale energy storage for renewable solar power and wind power.

Researchers working in the field of NIBs have focused their efforts on the exploration of stable and low-cost cathode materials, including Prussian blue,[3] $NaVPO_4$,[4] and $Na_2FePO_4F$.[5] However, the key problem in realizing NIBs is the lack of suitable negative electrodes, because graphite, a commercially well known anode material for LIBs, considered to be a failure as an anode in NIBs due to a lack of binary intercalation compound in the Na−C system and the large ionic size of the Na ion.[6] On the contrary, in recent work,[7] the reversible capacity of 100 mAh $g^{-1}$ was reported for a ternary graphite intercalation compound. However, the Na-storage capacity stated for graphite intercalation compound is not enough for high energy density NIBs. Moreover, only a few studies have been carried out on non-graphitic carbonous materials such as hard carbon due to their large interlayer distance and disordered structure,[8,9] as negative electrode materials have been found in the past. Stevens and Dahn reported an initial reversible capacity of hard carbon as high as 300 mAh $g^{-1}$.[8] However, some disadvantages are revealed for nongraphitic carbonaceous materials such as the poor rate performance and that the capacities delivered by hard carbon strongly depend on the method used for synthesis.[10] In addition, conversion type materials (transition metal oxides) have also been investigated as anode materials for Na-ion batteries.[11−13] However, none of these has demonstrated comparable performances for Na-ion batteries. Nevertheless, the continuous intensive efforts made to explore new anode

**Received:** May 14, 2015
**Accepted:** July 17, 2015
**Published:** July 17, 2015

DOI: 10.1021/acsami.5b04178
*ACS Appl. Mater. Interfaces* 2015, 7, 17226−17237

materials for sodium storage led to confirmation of the sodium-storage capability of Sn and Sb metal based Na-alloying materials.[11,14−19] Among these materials, Sn-based materials have received special attention because metallic Sn can yield a capacity as high as 847 mAh $g^{-1}$ from the alloying reaction ($4Sn + 15Na \rightarrow Na_{15}Sn_4$), while it has a low cost and is environmentally friendly.[20] However, an extremely large volume expansion occurs during the alloying reaction, leading to particle pulverization/exfoliation and rapid capacity fading of these materials.[16] Nevertheless, the tin oxide can achieve high specific capacities by acting as a conversion type as well as alloying material to store Na.[21−26] Therefore, it could be a potential anode material for Na-ion storage. Despite these advantages, tin oxide anodes have shown low capacities and poor capacity retention due to the swelling and shrinking of active material particles upon the insertion and extraction of $Na^+$ ions.[27] This particle volume change can further induce poor contact between the active materials and the electron conducting agents, leading to low electric and ionic conductivity. Thus, the specific capacity and calendar life of the tin oxide based anodes should be improved before they can be successfully employed in Na-ion batteries. To mitigate the pulverization and buffer the volume change, several approaches have been attempted, such as covering the material with a buffer layer[16,23] and reducing the particle size of the active material to nanoscale.[21,28] In particular, carbon (which can be obtained in a cost-effective way from various sources) has been considered as the most effective buffer material,[21−23,28] since the porous structure of carbon can easily provide housing to buffer the volume change to reduce the stress and improve the contact and conductivity of the material.

Herein, we report a simple and efficient approach to engineer carbon encapsulated $SnO_2$ porous structures as anode materials for Na ion batteries electrode. This work deals with the effect of the solvent used in the hydrothermal process, on the morphologies of $SnO_2$ nanostructures. Furthermore, attempts were made to decrease the particle size of the tin oxide and to enclose it in the amorphous carbon matrix. Ultrafine spherical nanoparticle of $SnO_2$ covered with carbon prepared in ethanol exhibited a high reversible capacity of 514 mAh $g^{-1}$ at a 0.1 C rate and an excellent cycling performance.

## ■ EXPERIMENTAL SECTION

**Material Synthesis.** Carbon coated $SnO_2$ nanostructures were synthesized using the hydrothermal oxidation of $SnCl_2{\cdot}2H_2O$) (Alfa-Aesar, 98%) in the presence of urea (Sigma-Aldrich, 99.5%), a reaction promoter, and polyvinylpyrrolidone (PVP) (Sigma-Aldrich; av mol wt, 40000), a carbon source. All chemicals were used as received without further purification. In a typical process, a solution (50 mL) was prepared by dissolving Sn precursor and urea with molar ratio 1:6 in three different solvents, viz., deionized (DI) water, ethylene glycol (EG), and ethanol (ET). The resulting blend was then stirred for 30 min before and after the addition of PVP. Subsequently, the precursor solutions were mixed thoroughly and reacted at 140 °C for 12 h in an 80 mL stainless steel autoclave with Teflon lining. The precipitate thus obtained was washed repeatedly for removal of $Cl^-$ impurities and dried overnight in a vacuum oven at 90 °C.

**Structural Characterization.** An X-ray diffractometer (XRD; D/MAX Ultima III, Rigaku, Tokyo, Japan) with Cu K$\alpha$ radiation was used to analyze the crystal structure of the synthesized materials. Thermogravimetric analysis (TGA; TGA-50 Shimadzu instrument) of the materials was carried out from room temperature to 750 °C with a ramp of 10 °C $min^{-1}$. Nitrogen adsorption and desorption isotherms (ASPA 2020, Micromeritics, Norcross, GA, USA) for the materials were measured at −196 °C to estimate the specific area of the materials. The specific surface area of the samples was calculated using the Brunauer−Emmett−Teller (BET) method. The microstructure and composition of the samples were observed using field emission scanning electron microscopy (FE-SEM, S-4700/EX-200, Hitachi) and transmission electron microscopy with an energy dispersive X-ray spectroscopy attachment (TEM-EDS, Tecnai G2, Philips−KBSI Gwangju Center).

**Electrochemical Characterization.** To investigate the electrochemical characteristics of carbon coated tin oxide nanostructures, the electrodes were fabricated using a slurry casting process. For casting, a slurry was prepared by mixing active material, carbon black, and binder at the weight ratio of 8:1:1. The slurry was then coated on Cu foil followed by drying at 90 °C for 6 h. The 2032 type coin cells were assembled in an Ar filled glovebox, with a working electrode (area, 1.5 $cm^{-2}$) punched from the cast electrode and Na metal as a counter and reference electrode. A solution of 1 M $NaPF_6$ dissolved in ethylene carbonate (EC) and dimethyl carbonate (DMC) at a volume ratio of 1:1 was used as the electrolyte. The electrochemical properties of the prepared electrodes were investigated using cyclic voltammetry (CV) in the potential range of 0.0−2.5 V vs $Na/Na^+$ at a scan rate of 0.1 mV $s^{-1}$ using a potentiostat (Gamry, PC750). In addition, the cells were galvanostatically charged and discharged from 0.005 to 2.5 V vs $Na/Na^+$ using an automatic battery cycler (Won-A-Tech-WBCS 3000). All experiments and tests were conducted at 25 °C.

## ■ RESULTS AND DISCUSSION

The crystal structure of the prepared powder was revealed by X-ray diffraction (XRD). Figure 1 shows XRD patterns of tin oxide/C composites prepared using the hydrothermal process. The tin oxide/C composite powder samples obtained were hereafter referred to as S-DI, S-EG, and S-ET considering the solvents used for the hydrothermal reaction, i.e., DI, EG, and ET, respectively. For samples S-DI and S-EG, the obtained high-intensity diffraction peaks were indexed to the tetragonal $SnO_2$ phase with a cassiterite structure (JCPDS 41-1445). It is also noted that the additional peak that occurred for both samples at 29.8° is indexed to the tetragonal SnO phases having

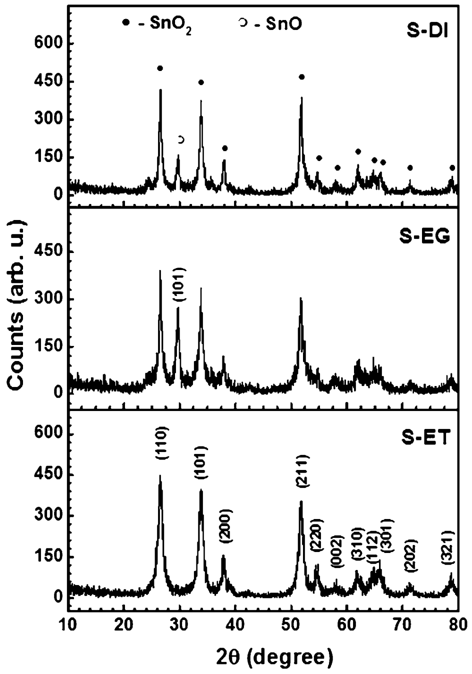

Figure 1. XRD patterns of tin oxide/carbon composite samples prepared in various solvents, DI water (S-DI), ethylene glycol (S-EG), and ethanol (S-ET).

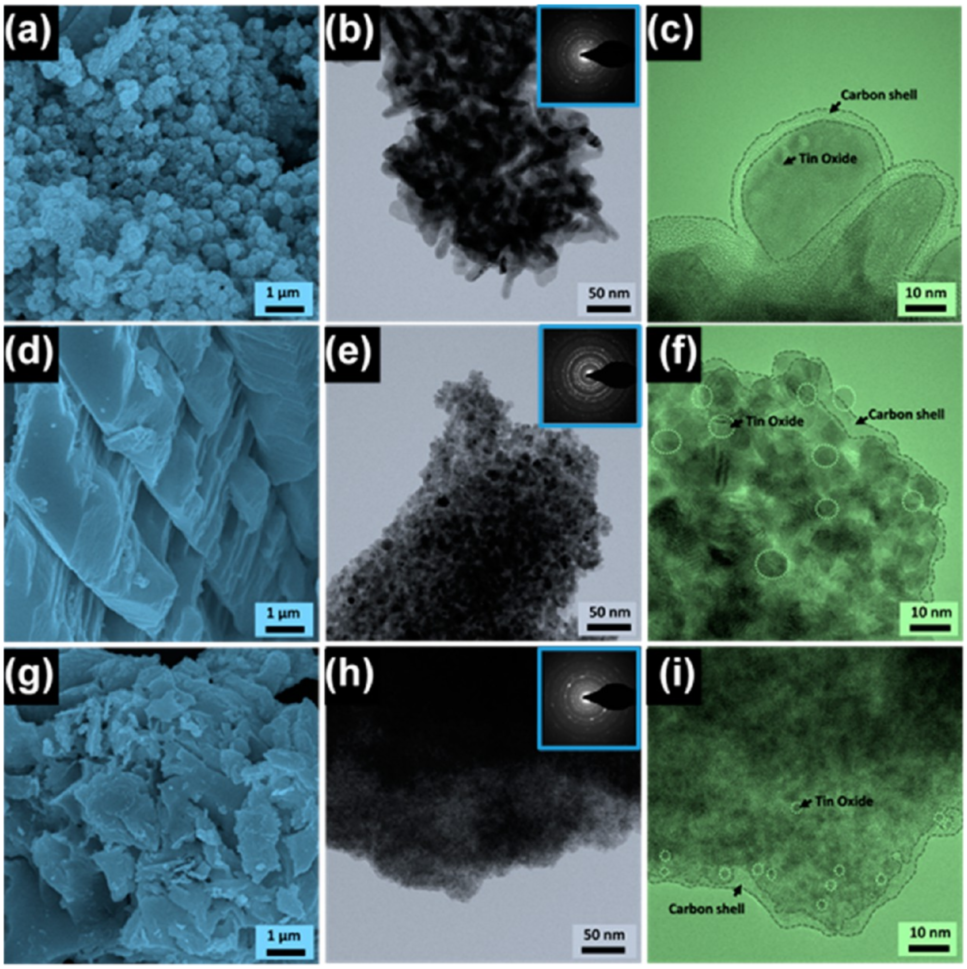

**Figure 2.** FE-SEM, TEM, and HR-TEM images of S-DI (a−c), S-EG (d−f), and S-ET (g−i), respectively. (Insets: SAED patterns for corresponding TEM images.)

a romarchite structure (JCPDS: 06-0395). On the other hand, all of the peaks of S-ET were indexed to the cassiterite structured tetragonal phase of $SnO_2$. No additional peak related to any other tin oxide phase or any other impurity, indicating the phase purity of the S-ET sample. It is obvious that all of the typical peaks are broadened and are of low intensity, demonstrating that the size of the $SnO_2$ particles is very small. In particular, the broadening of the peaks for sample S-ET is more apparent than that for S-DI and S-EG, suggesting the ultrafine nature of the particles for S-ET. The accurate weight percentage of $SnO_2$ and carbon in the prepared composite were evaluated to be 87:13, 91:9, and 77:23 for S-DI, S-EG, and S-ET, respectively, using TG analysis (Figure S1 in the Supporting Information).

The morphology of the products was detected using SEM and TEM. Figure 2a shows a typical low-magnification FE-SEM image of the postannealed S-DI sample. As illustrated, the sample consists of uniform spheres with an average diameter of 300 nm. The high-magnification image (Figure S2a in the Supporting Information) shows that the sphere is flower-like and exhibits a hierarchical structure. Further details on the morphological features of the S-DI sample were acquired from TEM and HR-TEM images, as shown in Figure 2b,c. It is clearly shown that several dozen nanosheets with a thickness of 20 nm and a width of 100 nm are connected to each other to form the flower-like spherical morphology. The surface of the sheets assembled into the flower-like hierarchical structures was very smooth, probably due to Ostwald ripening.[29] Furthermore, although these sheets were not highly close-packed, all of the microflowers maintained their integrity even after vigorous ultrasonic treatment for 30 min (TEM sample preparation), demonstrating the structural stability of the product. For the S-EG and S-ET samples, aggregated nanoparticles are observed in the SEM images, in Figure 2d,g, respectively. The TEM image for the S-EG and S-ET samples shows the quasi-spherical particles with average diameters of 10 and 4 nm, respectively. The particles observed by HR-TEM for both samples were composed of numerous single crystals (shown as white circles). Furthermore, from the HRTEM images of the S-EG and S-ET samples, it can be seen that the particles with uniform size were distributed evenly in the entire composite. The selected area electron diffraction (SAED) patterns in the inset of the TEM image (Figures 2b,e,h) demonstrate that the samples are polycrystalline and highly crystalline. The observed diffraction rings for S-DI, S-EG, and S-ET can be roughly indexed to tetragonal $SnO_2$. A closer inspection of all of the samples using HR-TEM (Figure 2c,f,i) reveal that the tin oxide particles are tightly encapsulated with an amorphous carbon layer. The carbon layer in the HR-TEM image is indicated by dotted lines. The thickness of the carbon encapsulation is observed to vary depending on the solvents used in the reaction during the synthesis process. For S-DI and S-ET, the $SnO_2$ particles were

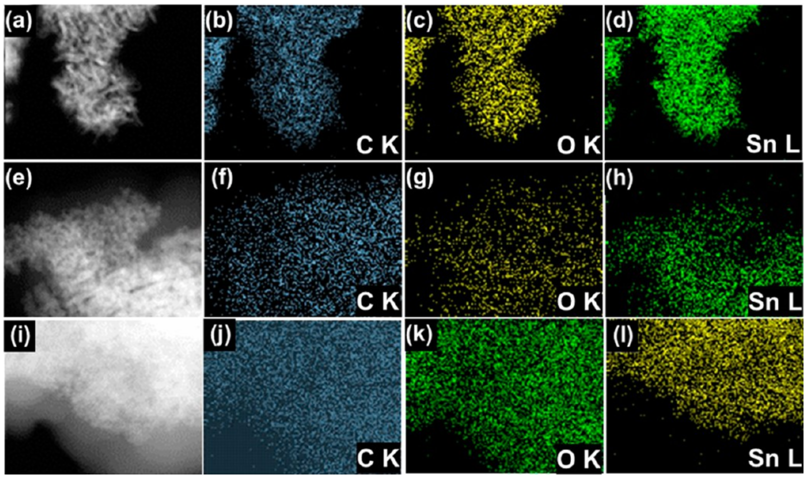

**Figure 3.** STEM, and carbon, oxygen, and tin elemental mapping images of S-DI (a−d), S-EG (e−h), and S-ET (i−l), respectively.

entirely covered with a thick carbon layer, while a thin carbon encapsulation is seen on the S-EG sample. Furthermore, the tin oxide samples were investigated for composition analysis using a TEM-EDAX tool. The STEM images and corresponding elemental mapping for $SnO_2$ materials are given in Figure 3a−l. The Sn and O were found to be the main elements in the samples. The presence of C on the entire surface of all of the samples originated from the PVP. The elemental mapping result supports the finding that the encapsulating layer detected was amorphous carbon, on closer inspection using HR-TEM. As previously reported, the carbon encapsulation for the Sn-based anodes could substantially improve the electrochemical performance of NIBs.[22,23,28,30]

The anticipated formation mechanism of carbon coated $SnO_2$ nanostructures in the hydrothermal process can be proposed based on the experimental observations, as illustrated in Figure 4. According to the figure, it is anticipated that the polymerization of the tin ions occurred by forming the complex with PVP during the initial phase of the reaction. In the later part, the concentration of the hydroxide ions starts to increase into the solution (reactions 1 and 2). This increase in the hydroxide ions is responsible for the initiation of the hydrolysis process, leading to the formation of tin hydroxide by decomposing the tin−PVP complex (reaction 3). Under the hydrothermal conditions, the tin hydroxide in the presence of the oxygen trapped in the hydrothermal reactor decomposed, and massive $SnO_2$ nuclei were formed in the nanocrystals, as given in reaction 4. In addition, according to the previous hydrothermal experiments,[31] the precursor used in the present work, i.e., $SnCl_2{\cdot}2H_2O$, can easily hydrolyze in aqueous solution producing $Sn(OH)_2$, leading to the formation of SnO, as given in the possible chemical reaction 5. This suggests that the $Sn(OH)_2$ formed during hydrothermal process in DI water can decompose to form $SnO_2$ and SnO, as confirmed in the XRD analysis (Figure 1). Further in the DI water, the formed nanocrystals undergo Oswald ripening to form the nanosheets. Finally, these nanosheets were self-assembled to build the flower-like hierarchical structures (Figure S2a). However, for S-EG, the aggregation and oriented growth of the nanocrystal resulted in the flower-like structure (Figure S2b in the Supporting Information). On the contrary, aggregation of the nanocrystal is only achieved for the S-ET samples (Figure S2c in the Supporting Information).

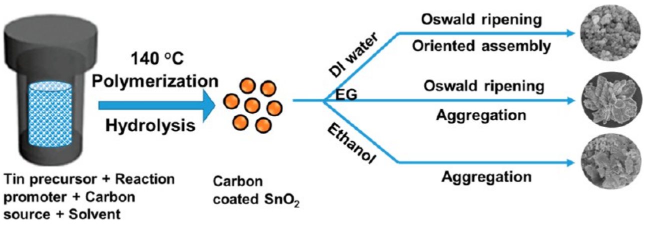

**Figure 4.** Proposed mechanism for the formation of various morphologies for tin oxide/carbon composites.

$$H_2NCONH_2 + H_2O \rightarrow 2NH_3 + CO_2 \tag{1}$$

$$NH_3 + H_2O \rightarrow NH_4^{+} + OH^{-} \tag{2}$$

$$Sn^{2+} + 2OH^{-} \rightarrow Sn(OH)_2 \tag{3}$$

$$Sn(OH)_2 + \frac{1}{2}O_2 \rightarrow SnO_2 + H_2O \tag{4}$$

$$Sn(OH)_2 \leftrightarrow SnO + H_2O \tag{5}$$

The nitrogen adsorption−desorption isotherms of the S-DI, S-EG, and S-ET samples were recorded at 77 K, as shown in Figure 5. The isotherms for the S-DI and S-EG materials were close to those of a type-III with H3 hysteresis (according to the International Union of Pure and Applied Chemistry (IUPAC) classification), indicative of a porous structure.[32] The hysteresis observed in the intermediate pressure range indicates the slit-like pores typically formed by the aggregation of plate-like particles, as observed for S-DI. Moreover, for S-ET, the isotherms were of close to type-IV. The size of the hysteresis loop is associated with the volume and connectivity of the pores. The hysteresis in the adsorption−desorption branch is indicative of a mesoporous structure. Moreover, the initial part of the isotherm is attributed to monolayer−multilayer adsorption. The specific area of the samples was analyzed from the $N_2$ adsorption−desorption curves using the BET method. The specific surface area and total pore volume of each sample are shown in Table 1. The table shows that the surface area values of S-DI and S-EG were less than those of the S-ET samples. This may be due to the formation of a porous structure with small connected particles during the hydrothermal process. The highest specific surface area observed for the S-ET sample was 47 $m^2\ g^{-1}$, while the lowest value for S-EG

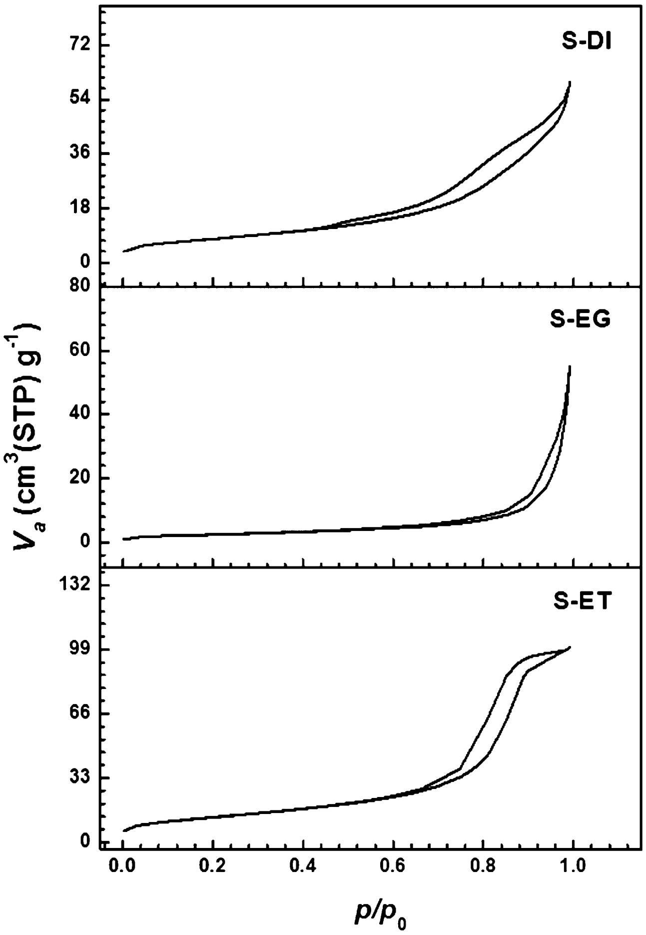

**Figure 5.** Nitrogen adsorption−desorption isotherms recorded at 77 K for S-DI, S-EG, and S-ET.

**Table 1. BET Surface Area, BJH Average Pore Diameter, and Total Pore Volume Calculated from $N_2$ Adsorption−Desorption Isotherms for Hydrothermally Prepared Tin Oxide Powders**

| sample name | surface area ($m^2$ $g^{-1}$) | av pore diam (nm) | total pore vol ($cm^3$ $g^{-1}$) |
|---|---|---|---|
| S-DI | 28.8 | 12.6 | 0.09 |
| S-EG | 8.7 | 36.8 | 0.08 |
| S-ET | 47 | 13.2 | 0.15 |

was 8.7 $m^2$ $g^{-1}$. Furthermore, the estimated total pore volumes of the S-DI, S-EG, and S-ET samples were 0.09, 0.06, and 0.15 $cm^3$ $g^{-1}$, respectively.

The size distribution as a function of pore diameter for all tin oxide/C composite powders was enumerated from the desorption curve using the Barrett−Joyner−Halenda (BJH) method and is presented in Figure S3 in the Supporting Information. The peaks with maximum at 10.7 and 16 nm were observed in the pore size distribution curves for the S-DI and S-ET samples, respectively. The pore size distribution curve for S-DI confirms the presence of a wide range of pores by exhibiting a broad peak, as shown in Figure S3 in the Supporting Information. Further, for S-ET, a narrow pore size of range 10−20 nm was evinced. In contrast, the S-EG sample exhibited peaks at ∼22, 43, and ∼77 nm, suggesting meso- and macroporosity of the materials. Referring to the values of pore size, pore volume, and surface area, the tin oxide sample with carbon encapsulation prepared with ethanol as a solvent could exhibit greater sodium storage. Moreover, it is well-documented that the material with large surface area can provide more locations and channels for fast $Na^+$-ion insertion/extraction into the electrode material. In addition, the existent porous structure not only can benefit the diffusion of the $Na^+$ ion but also can accommodate the volume changes during the alloying reaction ($Sn + xNa \rightarrow Na_xSn$) to maintain the structural integrity.

The sodium-storage ability of the carbon encapsulated tin oxide samples was evaluated from electrochemical measurements carried out at room temperature. The galvanostatic discharge−charge curves were recorded at the constant current rate of 0.1 C within the potential window of 0.005−2.5 V vs $Na/Na^+$, as shown in Figure 6. In the first discharge curve of S-DI, well-defined three slope regions were clearly observed: viz., region I, OCP to 1.1 V; region II, 1.1 to 0.3; and region III, 0.3 to 0.05 V. A similar nature of the discharge curve was demonstrated by Wang et al. for octahedral $SnO_2$ nanocrystals.[33] Accordingly, these three regions correspond to the three different reactions given as follows. Region I is ascribed to the Na-ion insertion into $SnO_2$ nanoparticles, as shown in reaction 6.

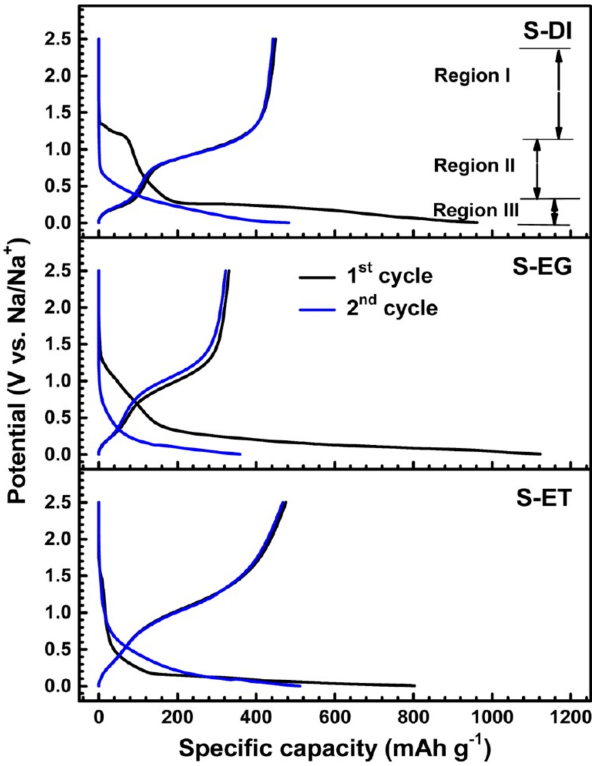

**Figure 6.** Potential profile for first and second galvanostatic discharge−charge curves for S-DI, S-EG, and S-ET at a rate of 0.1 C.

$$SnO_2 + Na^+ + e^- \rightarrow NaSnO_2 \quad (6)$$

Region II corresponds to the reduction of $SnO_2$ to metallic Sn by forming sodium oxide:

$$SnO_2 + 4Na^+ + 4e^- \rightarrow Sn + 2Na_2O \quad (7)$$

Region III can be assigned to the Na−Sn alloying reaction and the formation of a solid−electrolyte interface (SEI).[34,35]

$$\mathrm{Sn} + x\mathrm{Na}^+ + xe^- \leftrightarrow \mathrm{Na}_x\mathrm{Sn} \qquad (8)$$

On the contrary, for S-EG and S-ET, regions I and II seem to be merged to give only two distinct regions, indicating that sodium is being stored following reactions 7 and 8.

The charge curve for all of the samples exhibit two well-defined regions: from 0.005 to 0.7 V and from 0.7 to 1.4 V. Herein, the low-potential region indicates the dealloying process of $Na_{3.75}Sn$, while the reaction occurring at higher potential is ascribed to the reaction between Sn and $Na_2O$ to regenerate $SnO_2$. Moreover, the first discharge capacities obtained for S-DI, S-EG, and S-ET were 992, 977, and 1014 mAh $g^{-1}$, respectively. Considering reactions 7 and 8, the theoretical first discharge capacity is 1378 mAh $g^{-1}$. However, the lower discharge capacities obtained in the current case for carbon encapsulated $SnO_2$ compared with theoretical values can be attributed to the incomplete alloying process due to kinetic difficulty of the Na−Sn alloying reaction. Moreover the contribution of carbon in the composite is much less as determined from the galvanostatic charge−discharge of carbon (Supporting Information Figure S4) obtained with the same procedure as explained earlier for $SnO_2$/C composite using only carbon precursor. The reversible capacity exhibited by bare carbon is only 50 mAh $g^{-1}$ with Coulombic efficiency merely 20%. This might be the reason for attaining smaller first discharge capacities with an increase in the carbon contained in the composites. The increased amount of carbon can reduce the amount of active material (i.e., $SnO_2$) in the composite resulting in less charge storage in the composite. Furthermore, the charge capacities obtained for the S-DI, S-EG, and S-ET samples were 456, 297, and 514 mAh $g^{-1}$ having conversion efficiencies of 46%, 30.4%, and 50.7%, respectively. The values obtained for the Coulombic efficiencies for the $SnO_2$/C composite are in agreement with the earlier reports.[28] The initial low Columbic efficiency could be attributed to the formation of a SEI layer in the first cycle. In addition, according to recent work[24] on the investigation of phase transformation of $SnO_2$ carbon composite during sodiation/desodiation, the low value of Coulombic efficiency is ascribed to the partial reversible conversion reaction ($\mathrm{Sn} + 2\mathrm{Na_2O} \rightarrow \mathrm{SnO_2} + 4\mathrm{Na}^+ + 4e^-$). This can be further related to the irreversible binding of Na with oxygen. In the second charge−discharge profile for all of the samples, the distinctive discharge plateaus are absent, exhibiting the similar discharge behavior. In fact, this is the characteristic potential profile features of crystalline tin as reported earlier.[30] On the other hand, for charge reaction, the two distinct plateaus are seen in the second potential profile, indicating sodium-ion release follows a series of different faradaic processes; this desodiation mechanism will be further confirmed with the XRD and XPS analysis.

The electrochemical reactions of the carbon encapsulated tin oxide nanocomposites were further evaluated by cyclic voltammetry (CV). Figure 7 shows the first three cyclic voltammograms of the $SnO_2$/C nanocomposite electrodes conducted at a scan rate of 0.1 mV $s^{-1}$ from the 2.5 to 0 V vs $Na/Na^+$. As shown in Figure 7, for S-EG, a large irreversible current peak between 0.01 and 1.6 V is observed in the first cathodic scan. This peak is ascribed to the transformation of $SnO_2$ into Sn at the first discharge process.[22] Moreover, this irreversibility is possibly instigated from the irreversible reactions between $Na^+$ and the active materials and the formation of the SEI layer on the electrode surface.[16] In the CV profile for S-DI and S-ET, a broad peak starts at 1 V with an increase in CV current until the full discharge. The peaks appearing at approximately 0.6 V are ascribed to the oxide conversion reaction, whereas the cathodic portion with increased intensity can be attributed to the alloying reaction between Sn and Na to form $Na_xSn$ alloy and the Na-ion insertion into the carbon. According to the Na−Sn binary alloy phase diagrams and previous reports, $\alpha$-NaSn, $Na_9Sn_4$, $Na_3Sn$, and $Na_{15}Sn_4$ are the main stable phases.[36,37] It is presumed that the reduction peak at potential 0.4 V could correspond to the formation of a SEI layer on the electrode surface and alloying of metallic Sn into $\alpha$-NaSn.[24] On the other hand, the reduction peak at lower potential (0.02 V) is assigned to the formation of a single phase of $Na_3Sn$ and $Na_{15}Sn_4$, together with the adsorption of $Na^+$ on the carbon surface. In the anodic scan, three distinct peaks were observed at approximately 0.27, 0.6, and 0.94 V. These peaks indicate the phase transition during the dealloying process. Peaks at 0.27 and 0.6 V could mainly belong to the dealloying reaction of $Na_{15}Sn_4$ to $Na_9Sn$, then $\alpha$-NaSn and to $NaSn_5$, while the second hump peaking at 0.95 V originates due the conversion reaction, i.e., formation of oxide.[24] Under continuous scan, the CV profiles of the following cycles exhibit the distinct pair of cathodic and anodic peaks with comparable intensities, suggesting the highly reversible electrochemical reactions in $SnO_2$/C nanocomposites, promising extended cycle life.

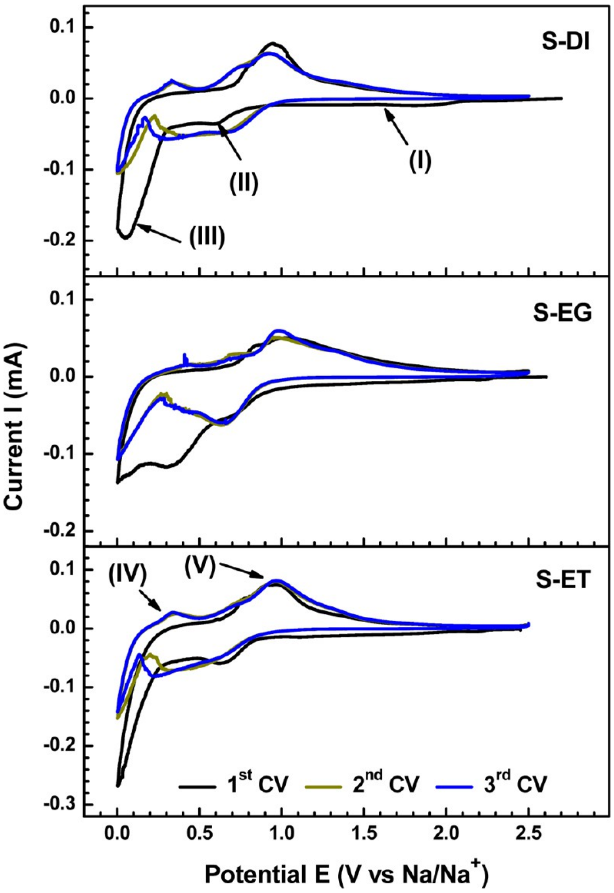

**Figure 7.** First three cyclic voltammograms of the $SnO_2$/C nanocomposite electrodes conducted at a scan rate of 0.1 mV $s^{-1}$ from the open circuit voltage to 0 V vs $Na/Na^+$.

The XRD characterizations were performed to fully charged and discharged electrodes to find the exact mechanism of Na storage in the $SnO_2$/C composite. As illustrated in Figure 8a,

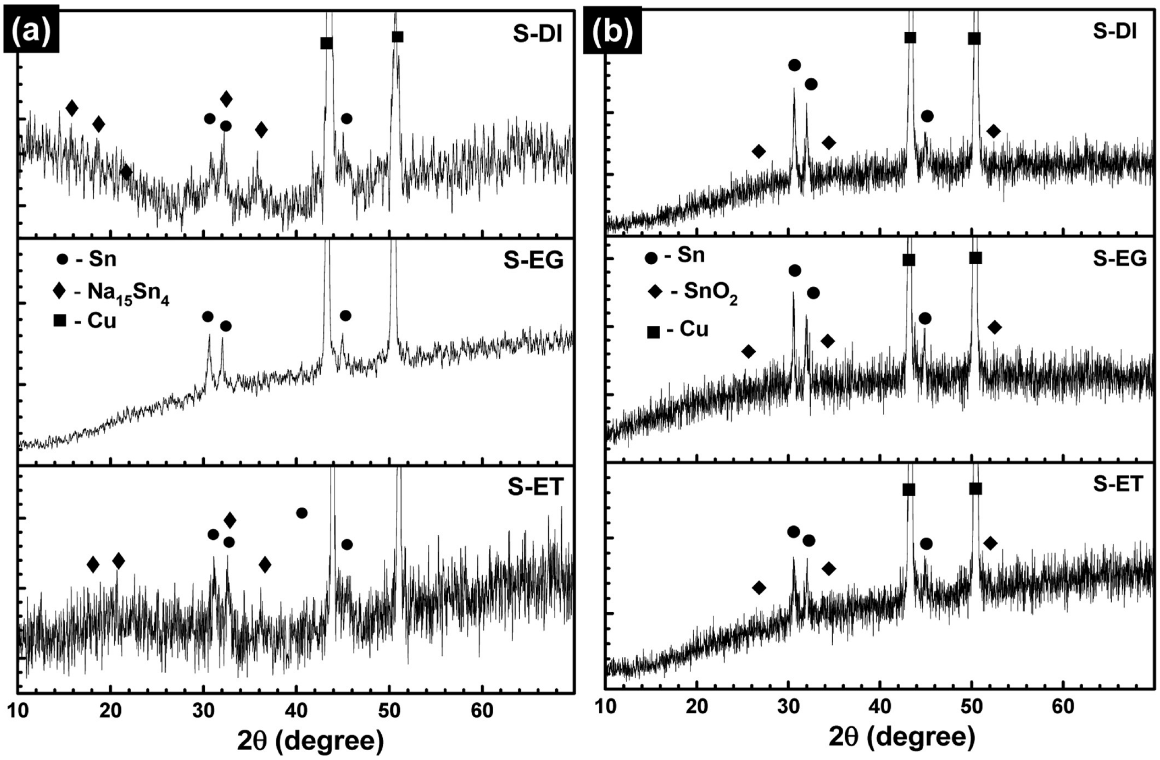

**Figure 8.** XRD patterns of the $SnO_2$/C composite electrodes in full discharge (a) and full recharge state.

the peaks related to the crystalline Sn and $Na_{15}Sn$ phase were observed for S-DI and S-ET samples, whereas the peaks related to only crystalline Sn were seen in S-EG. The presence of Sn peaks in the fully discharged electrode suggest the incomplete alloying and absence of peaks corresponding to tin oxide, indicating the complete conversion of the material.[25] This incomplete alloying of Sn due to lower diffusion of Na and sluggish interfacial reaction kinetics is the basis of lower capacity at first discharge for the $SnO_2$/C composite. The poor diffusion kinetics and ionic conductivity of the $Na_2O$ shell with Sn as core formed during the conversion reaction can also be a factor that impedes the Sn alloying process.[26] In addition, a solid SEI layer formed on the surface of the electrode can also reduce the sodiation rates and hence the discharge capacities. To stabilize and improve the SEI layer, it is suggested to use fluoroethylene carbonate (FEC) as an additive in the electrolyte, to enhance the Coulombic efficiency and cycle life of the material in NIBs.[22,30,38,39] After analyzing the discharge electrode, it is concluded that the most favorable Na-storage process is conversion reaction, while the alloying process is incomplete and has a kinetic barrier.[24,25] Furthermore, the charged electrodes also were investigated with XRD; the obtained pattern is given in Figure 8b. The peaks related to the metallic Sn were observed in the charged electrode, while the peaks related to $Na_{15}Sn$ alloy are diminished. It is anticipated that the Sn could convert to tin oxide during the charge process. However, the XRD pattern of the charged electrode does not show any peaks related to SnO or $SnO_2$; this can be due to formation of nanocrystalline tin oxide or suppression of peaks due to a high intensity of Sn peaks. The formation of oxide is further confirmed by analyzing the charged electrode (S-DI) by XPS (Figure 9 and Figure S5). The changed oxidation state of $Sn^0$ (in metallic Sn) to $Sn^{4+}$ (in $SnO_2$) after desodiation in Sn 3d core level XPS spectra suggest the conversion of metallic tin to its oxide, specifying the reverse conversion reaction in the charge process. In prior sodiation, the oxidation state of Sn is changed to metallic $Sn^0$ from its $Sn^{4+}$ state due to oxide conversion reaction. The presence of Sn on the charged electrode is ascribed to the incomplete conversion reaction due to strong bonding between O and Na. The observed charge-storage mechanism for the $SnO_2$/C composite in the present case is in good agreement with the

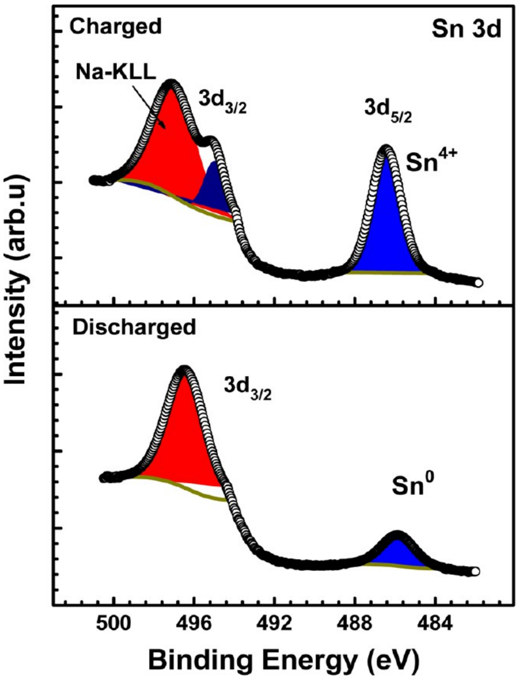

**Figure 9.** Sn 3d XPS spectra of $SnO_2$/C composite (S-DI) electrode after first discharge and first charge.

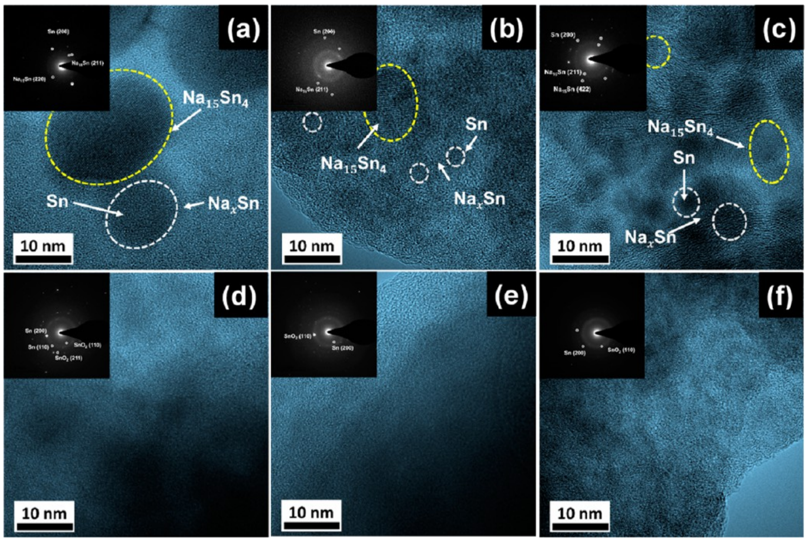

**Figure 10.** HR-TEM images of $SnO_2$/C electrodes during first cycling for (a, d) S-DI, (b, e) S-EG, and (c, f) S-ET after first discharge and charge, respectively. (Insets: SAED patterns for corresponding TEM images.)

phase transition mechanism given for the $SnO_2$/C composite in a limited number of previous reports.[24,25]

To support the XRD results, TEM analysis of the $SnO_2$/C electrodes after full discharge and charge was carried and the results were summarized in Figure 10. The discharge reaction for all of the composite electrodes resulted in the complete conversion of $SnO_2$ and limited alloying of Sn, showing the crystalline $Na_{15}Sn_4$ and the metallic Sn surrounded by amorphous Na$x$Sn phases in the HRTEM images (Figure 10a–c). The SAED patterns of the electrode shown in the inset of the HRTEM image validate the formation of $Na_{15}Sn_4$, specifying alloying of Sn, even though the alloying process is not completed. On charge the reverse conversion process is also validated by SAED patterns. The particle size for S-DI decreased to 20 nm due to pulverization of the materials during sodiation–desodiation (Figure 10d). The XRD and TEM results authenticate the mechanism of conversion and alloying in the $SnO_2$/C composite. These results are in agreement with those reported recently.[24,33] As displayed in Figure 10e, in S-EG, agglomeration of particles starts to occur because the thin carbon coating is unable to accommodate the volume change. On the contrary, particles with size below 10 nm and evenly distributed in the carbon matrix can maintain the pristine structure during insertion and desertion of Na ion (Figure 10 f). From these results one can expect good cycling life for S-ET, while S-EG can show capacity fading with cycle number.

To better understand the electrochemical behavior of all of the synthesized carbon encapsulated tin oxide samples under the various current rates, we also investigated their C-rate performances as shown in Figure 11. Furthermore, to avoid the induced effect due to the activation of the electrode, the cells cycled at 0.1 C for 10 cycles were used for a rate capability test. All of the electrodes were operated at various C-rates between 0.1 and 5 C. It can be clearly seen that the S-ET electrode shows a better rate capability than the S-DI and S-EG electrodes. However, at a higher current rate of 5 C, the S-ET electrode delivered a high reversible capacity of 134 mA h g$^{-1}$, whereas only 65 mA h g$^{-1}$ and 11 mA h g$^{-1}$ were delivered by the S-DI and S-EG electrodes, respectively. To the best of the authors' knowledge, the sodium storage in tin oxide at such a high current rate of 5 C has rarely been reported in the literature. The capacity obtained for the S-ET electrode at a current rate of 1 C (304 mA h g$^{-1}$) is higher than the earlier reported values of $SnO_2$-based composites.[21,22,40] More importantly, when the testing current returned to a lower current rate of 0.1 C, the discharge/charge capacities recovered to the same levels that were initially shown at that particular rate.

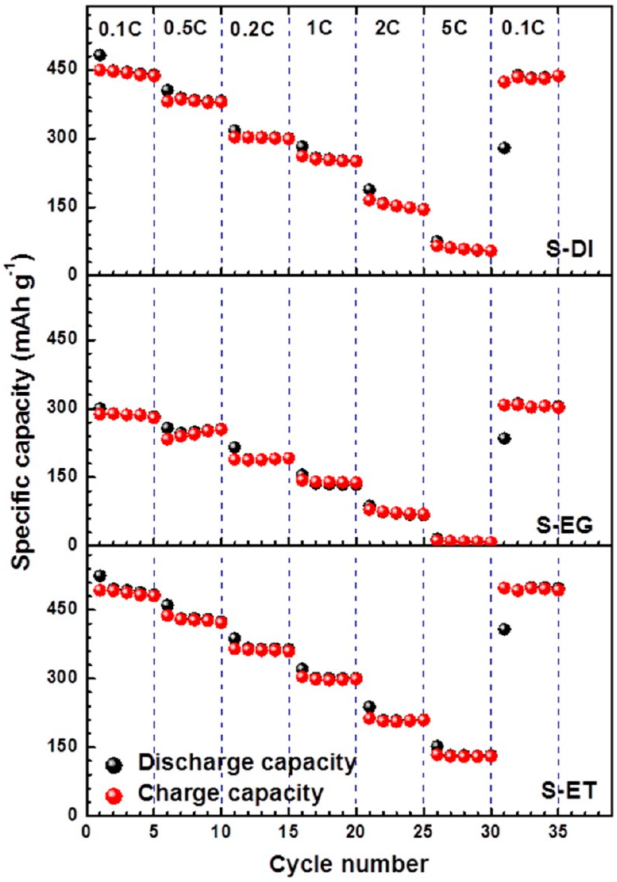

**Figure 11.** Rate performance of S-DI, S- EG, and S-ET nanocomposites at applied various current rates.

In order to further investigate the effect of high current rate on the long-range cyclability of the flower-like S-DI, S-EG, and S-ET electrodes, we further evaluated the cyclability of all of the electrodes at 0.1 C for the first five cycles (for activation) and at a high current rate of 0.5 C for the remaining cycles, as shown in Figure 12. It can be clearly seen that the S-ET and S-DI electrodes show high capacity and excellent cyclability up to 200 cycles with almost 95% and 100% specific capacity retention, respectively, among the investigated electrodes. Moreover, the S-ET and S-DI electrodes retained the reversible capacities of 413 and 362 mA h g$^{-1}$ from their initial charge capacities of 433 and 360 mA h g$^{-1}$ after 200 cycles, respectively, whereas the S-EG electrode retained only 109 mA h g$^{-1}$ after the same cycling. The excellent electrochemical performance of S-DI and S-ET can be attributed to their large specific surface areas and porous nature, which are helpful for the electrolyte diffusion and intercalation of the Na$^+$ ions into the active material. Furthermore, the pores can provide the space to accommodate the volume change and prevent electronic disconnections in the electrode materials during the sodiation and desodiation processes. It is important to note that in the present work the SnO$_2$/C composite exhibited excellent cycling life without using the FEC additive. According to the previous studies, FEC can be used as an additive in carbonate-based electrolyte to form stable and improved SEI to increase the initial Coulombic efficiency and further enhance the cycle life of electrodes in SIBs.[30,38,39] With the use of FEC, one can anticipate a boost in the electrochemical performance with extended cycle life for the SnO$_2$/C composite. Furthermore, Figure 12 also shows the Columbic efficiencies of all of the investigated electrodes up to 200 cycles. It can be clearly observed that all of the investigated electrodes show high Columbic efficiency of more than 98% up to 200 cycles.

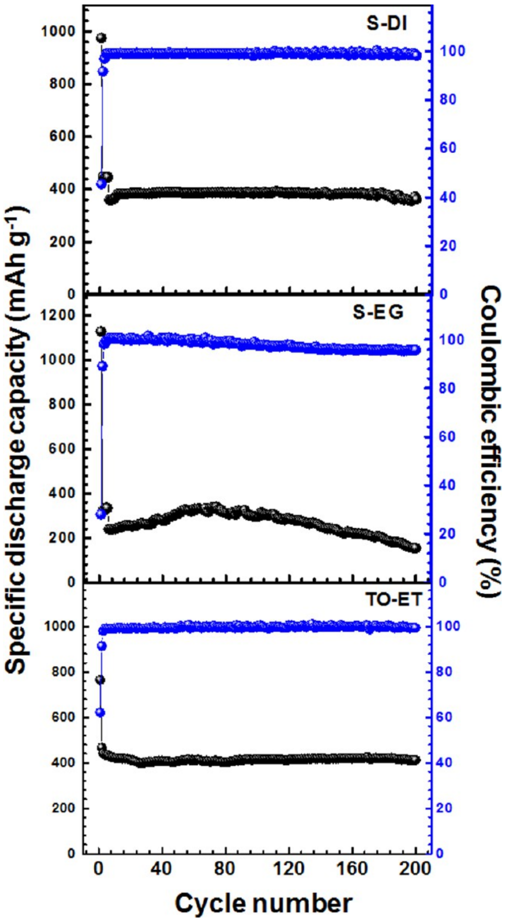

**Figure 12.** Discharge capacities and Coulombic efficiencies vs cycle number of S-DI, S-EG, and S-ET nanocomposites at applied current rate of 0.5C.

The superior electrochemical performance of the S-ET electrode could be due to its porous nature and higher surface area, which provides easy accessibility of electrolytes and empty spaces to accommodate volume change during alloying reaction. However, in order to understand the electrochemical performance of the S-DI, S-EG, and S-ET electrodes, the morphology change was examined after electrochemical cycling. Figure 13 shows the ex situ SEM image of the S-DI, S-EG, and S-ET electrodes after 200 cycles. To perform ex situ SEM studies, the cycled electrode were initially separated from the cell in an argon filled glovebox. The electrodes were then

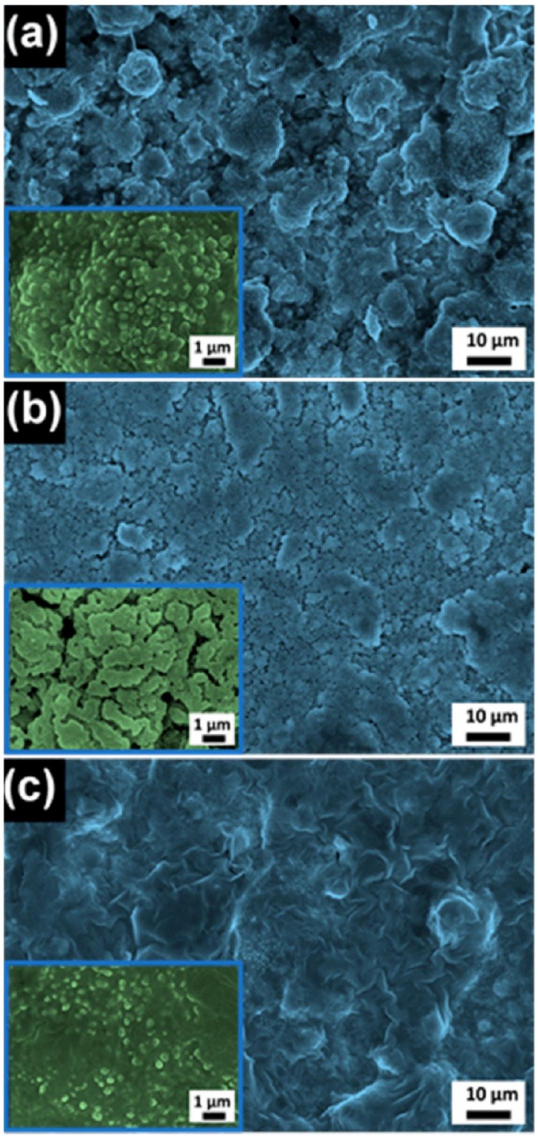

**Figure 13.** Ex situ FE-SEM images (1*k* magnification) of the SnO$_2$/C nanocomposite electrode (a) S-DI, (b) S-EG, and (c) S-ET after 200 cycles of the Na insertion−desertion test. (Insets: FESEM images at 10*k* magnification of the same electrode.)

washed thoroughly with the solvent, dimethyl carbonate, to remove the electrolyte salt. They were then dried overnight at 80 °C in a vacuum oven. Comparing the FE-SEM images of the S-DI and S-ET electrodes before cycling as shown in Figure S6a,c in the Supporting Information and the cycled electrode in Figure 13a,c, no obvious changes are observed after repeated charge/discharge cycles, except the smooth SEI layer formed on S-DI and S-ET. The FE-SEM images clearly show the smooth microstructure of the electrodes, demonstrating that the electrodes remain intact and unchanged during electrochemical cycling except for a slight increase in particle size. The larger particle size is a result of stresses caused by large charge/discharge volume change. The absence of capacity fading in the S-DI and S-ET electrodes can be attributed to the crack free and strongly connected electrode morphology of the electrodes which remains unbroken throughout the cycling. On the other hand, several cracks and loosely connected particles were observed for S-EG (Figure 13c), which could be attributed to the capacity fading (up to 57%) after 200 cycling.

The electrochemical impedance spectroscopy (EIS) was further used to understand the different electrochemical behaviors between the $SnO_2$/C nanocomposite electrodes as shown in Figure 14. The Nyquist plots were fitted by the equivalent circuit presented in the inset of Figure 14, where $R_e$ represents the electrolyte and ohm resistance, $R_f$ and $Q_1$ represent the surface film resistance and the relax capacitance, respectively, $R_{ct}$ and $Q_2$ represent the charge transfer resistance and the double layer capacitance, respectively, and $Z_w$ is the Na-ion bulk diffusion resistance. As seen in Figure 14 and Table 2, different behaviors in $R_{ct}$ are observed between S-DI, S-EG, and S-ET. Comparing the values of $R_{ct}$ and $R_f$ for all of the electrodes after first discharge, for S-DI and S-ET, much lower $R_{ct}$ values and smaller changes were observed in $R_{ct}$ than those for S-EG. The complete cover of carbon and its conducting effect is responsible for the lower $R_{ct}$ value of S-DI and S-ET, while the dispersing and fixing effects of carbon for $SnO_2$ can explain the smaller changes in $R_{ct}$ during cycling. These EIS results agree well with the enhanced electrochemical performance of S-DI and S-ET. For S-EG, although a similar SEI layer facilitates rapid Na-ion diffusion, the electron transfer remains difficult due to cracks formed by pulverization during cycling (Figure 13b). A low and stable $R_f$ is observed for all $SnO_2$/C nanocomposites, indicating the construction of a stabilized and thin SEI layer for the S-DI, S-EG, and S-ET electrodes. The stabilized SEI layer can stabilize the electrode/electrolyte interface by suppressing the continuous electrolyte decomposition and the growth of the SEI layer.[41] Therefore, the presence of the stabilized and thin SEI layer also contributes to the excellent cycling stability and rate capability of S-DI and S-ET. These results suggest that the excellent electrochemical performance of S-ET is related both to the unique microstructure of the hybrid and to the formation of a desirable SEI layer.

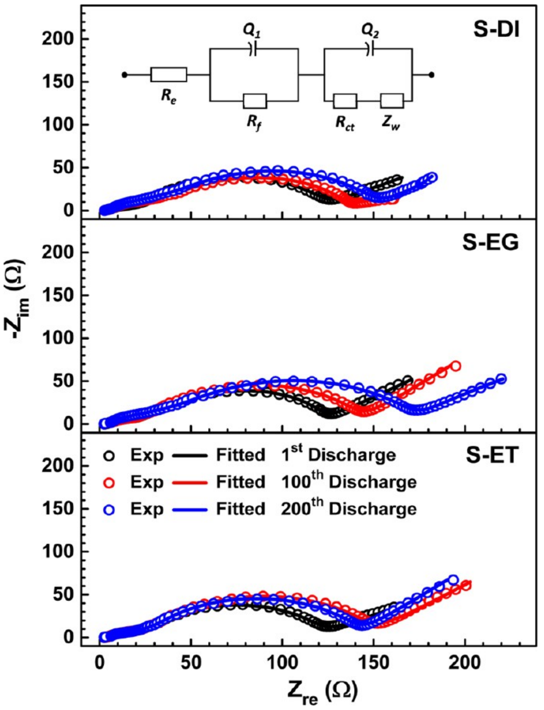

**Figure 14.** Electrochemical impedance analysis and Nyquist plots after first, 100th, and 200th cycles of reversible sodium storage for S-DI, S-EG, and S-ET nanocomposite electrodes. (Inset: equivalent circuit for the fitting.)

**Table 2. Electrolyte Resistance ($R_e$), SEI Film Resistance ($R_f$), and Charge Transfer Resistance ($R_{ct}$) Calculated from Nyquist Plots after Different Cycles for Carbon Encapsulated Tin Oxide Nanocomposites**

| sample name | cycle no. | $R_e$ (Ω) | $R_f$ (Ω) | $R_{ct}$ (Ω) |
|---|---|---|---|---|
| S-DI | 1 | 2.239 | 31.757 | 84.003 |
| | 100 | 2.745 | 33.98 | 101.58 |
| | 200 | 3.209 | 36.34 | 116.202 |
| S-EG | 1 | 2.592 | 33.79 | 107.569 |
| | 100 | 3.038 | 35.358 | 123.779 |
| | 200 | 3.735 | 37.463 | 179.83 |
| S-ET | 1 | 2.615 | 32.716 | 84.042 |
| | 100 | 2.78 | 34.18 | 102.443 |
| | 200 | 3.28 | 36.22 | 109.46 |

## CONCLUSIONS

In summary, carbon encapsulated tin oxide nanocomposites produced in ethanol as an anode for sodium-ion batteries overcomes the challenge of cycle life by maintaining the high capacity over 400 mAh $g^{-1}$ at 0.5 C for 200 cycles. The enhanced rate capability of the electrode material is achieved by improving the electronic conductivity using a carbon buffer. The significant improvement in the reversibility of the $SnO_2$/C electrode in Na-ion batteries is a direct outcome of its tailored properties including a high surface area, which is the key for easy and fast sodiation and desodiation reactions and porosity that enables good diffusion of Na-ions and electrolytes to the active sites. The present investigation is important as it demonstrates that the performance of the anode for Na-ion batteries can be thoroughly enriched by engineering the microstructure. Further improvements can also be achieved by employing new electrolytes and additives that offer high conversion (Columbic) efficiencies.

## ASSOCIATED CONTENT

### Ⓢ Supporting Information

The Supporting Information is available free of charge on the ACS Publications website at DOI: 10.1021/acsami.5b04178.

TGA curves, SEM micrographs, BJH pore size distribution curve for $SnO_2$/C composite, galvanostatic discharge−charge curve for baseline carbon, XPS analysis of discharged and charged $SnO_2$/C electrode, and SEM micrographs of pristine $SnO_2$/C composite electrodes (PDF).

## ■ AUTHOR INFORMATION

### Corresponding Author

*Tel.: +82-62-530-1704. Fax: +82-62-530-1699. E-mail: parkcj@jnu.ac.kr.

### Notes

The authors declare no competing financial interest.

## ■ ACKNOWLEDGMENTS

This work was supported by the Ministry of Education, Korea, under the Basic Science Research Program of the National Research Foundation of Korea (NRF; Grant No. 2015R1D1A3A01019399) and by the Ministry of Trade, Industry & Energy (MOTIE), Korea, under the Energy Efficiency & Resources Core Technology Program of the Korea Institute of Energy Technology Evaluation and Planning (KETEP; Grant No. 20112020100110/KIER B5-2592). In addition, we are grateful to the Korea Basic Science Institute (KBSI), Gwangju Centre for providing the HR-TEM facility.

## ■ REFERENCES

(1) Kang, B.; Ceder, G. Battery Materials for Ultrafast Charging and Discharging. *Nature* **2009**, *458*, 190−193.

(2) Palomares, V.; Serras, P.; Villaluenga, I.; Hueso, K. B.; Carretero-Gonzalez, J.; Rojo, T. Na-Ion Batteries, Recent Advances and Present Challenges to Become Low Cost Energy Storage Systems. *Energy Environ. Sci.* **2012**, *5*, 5884−5901.

(3) Lu, Y.; Wang, L.; Cheng, J.; Goodenough, J. B. Prussian Blue: A New Framework of Electrode Materials for Sodium Batteries. *Chem. Commun.* **2012**, *48*, 6544−6546.

(4) Lu, Y.; Zhang, S.; Li, Y.; Xue, L.; Xu, G.; Zhang, X. Preparation and Characterization of Carbon-Coated $NaVPO_4F$ as Cathode Material for Rechargeable Sodium-Ion Batteries. *J. Power Sources* **2014**, *247*, 770−777.

(5) Law, M.; Ramar, V.; Balaya, P. Synthesis, Characterisation and Enhanced Electrochemical Performance of Nanostructured $Na_2FePO_4F$ for Sodium Batteries. *RSC Adv.* **2015**, *5*, 50155.

(6) Jache, B.; Adelhelm, P. Use of Graphite as a Highly Reversible Electrode with Superior Cycle Life for Sodium-Ion Batteries by Making Use of Co-Intercalation Phenomena. *Angew. Chem., Int. Ed.* **2014**, *53*, 10169−10173.

(7) Ge, P.; Fouletier, M. Electrochemical Intercalation of Sodium in Graphite. *Solid State Ionics* **1988**, *28−30* (Part 2), 1172−1175.

(8) Stevens, D. A.; Dahn, J. R. High Capacity Anode Materials for Rechargeable Sodium-Ion Batteries. *J. Electrochem. Soc.* **2000**, *147*, 1271−1273.

(9) Thomas, P.; Billaud, D. Sodium Electrochemical Insertion Mechanisms in Various Carbon Fibres. *Electrochim. Acta* **2001**, *46*, 3359−3366.

(10) Ponrouch, A.; Goñi, A. R.; Palacín, M. R. High Capacity Hard Carbon Anodes for Sodium Ion Batteries in Additive Free Electrolyte. *Electrochem. Commun.* **2013**, *27*, 85−88.

(11) Dahbi, M.; Yabuuchi, N.; Kubota, K.; Tokiwa, K.; Komaba, S. Negative Electrodes for Na-Ion Batteries. *Phys. Chem. Chem. Phys.* **2014**, *16*, 15007−15028.

(12) Hariharan, S.; Saravanan, K.; Ramar, V.; Balaya, P. A Rationally Designed Dual Role Anode Material for Lithium-Ion and Sodium-Ion Batteries: Case Study of Eco-Friendly $Fe_3O_4$. *Phys. Chem. Chem. Phys.* **2013**, *15*, 2945−2953.

(13) Wen, J.-W.; Zhang, D.-W.; Zang, Y.; Sun, X.; Cheng, B.; Ding, C.-X.; Yu, Y.; Chen, C.-H. Li and Na Storage Behavior of Bowl-Like Hollow $Co_3O_4$ Microspheres as an Anode Material for Lithium-Ion and Sodium-Ion Batteries. *Electrochim. Acta* **2014**, *132*, 193−199.

(14) Doeff, M. M.; Ma, Y.; Visco, S. J.; De Jonghe, L. C. Electrochemical Insertion of Sodium into Carbon. *J. Electrochem. Soc.* **1993**, *140*, L169−L170.

(15) Xu, Y.; Zhu, Y.; Liu, Y.; Wang, C. Electrochemical Performance of Porous Carbon/Tin Composite Anodes for Sodium-Ion and Lithium-Ion Batteries. *Adv. Energy Mater.* **2013**, *3*, 128−133.

(16) Xiao, L.; Cao, Y.; Xiao, J.; Wang, W.; Kovarik, L.; Nie, Z.; Liu, J. High Capacity, Reversible Alloying Reactions in SnSb/C Nanocomposites for Na-Ion Battery Applications. *Chem. Commun.* **2012**, *48*, 3321−3323.

(17) Qian, J.; Chen, Y.; Wu, L.; Cao, Y.; Ai, X.; Yang, H. High Capacity Na-Storage and Superior Cyclability of Nanocomposite Sb/C Anode for Na-Ion Batteries. *Chem. Commun.* **2012**, *48*, 7070−7072.

(18) Kim, J.-C.; Kim, D.-W. Synthesis of Multiphase SnSb Nanoparticles-on-$SnO_2$/Sn/C Nanofibers for Use in Li and Na Ion Battery Electrodes. *Electrochem. Commun.* **2014**, *46*, 124−127.

(19) Qu, B.; Ma, C.; Ji, G.; Xu, C.; Xu, J.; Meng, Y. S.; Wang, T.; Lee, J. Y. Layered $SnS_2$-Reduced Graphene Oxide Composite − a High-Capacity, High-Rate, and Long-Cycle Life Sodium-Ion Battery Anode Material. *Adv. Mater.* **2014**, *26*, 3854−3859.

(20) Ellis, L. D.; Hatchard, T. D.; Obrovac, M. N. Reversible Insertion of Sodium in Tin. *J. Electrochem. Soc.* **2012**, *159*, A1801−A1805.

(21) Zhang, Y.; Xie, J.; Zhang, S.; Zhu, P.; Cao, G.; Zhao, X. Ultrafine Tin Oxide on Reduced Graphene Oxide as High-Performance Anode for Sodium-Ion Batteries. *Electrochim. Acta* **2015**, *151*, 8−15.

(22) Wang, Y.-X.; Lim, Y.-G.; Park, M.-S.; Chou, S.-L.; Kim, J. H.; Liu, H.-K.; Dou, S.-X.; Kim, Y.-J. Ultrafine $SnO_2$ Nanoparticle Loading onto Reduced Graphene Oxide as Anodes for Sodium-Ion Batteries with Superior Rate and Cycling Performances. *J. Mater. Chem. A* **2014**, *2*, 529−534.

(23) Su, D.; Ahn, H.-J.; Wang, G. $SnO_2$@Graphene Nanocomposites as Anode Materials for Na-Ion Batteries with Superior Electrochemical Performance. *Chem. Commun.* **2013**, *49*, 3131−3133.

(24) Ding, J.; Li, Z.; Wang, H.; Cui, K.; Kohandehghan, A.; Tan, X.; Karpuzov, D.; Mitlin, D. Sodiation Vs. Lithiation Phase Transformations in a High Rate - High Stability $SnO_2$ in Carbon Nanocomposite. *J. Mater. Chem. A* **2015**, *3*, 7100−7111.

(25) Li, Z.; Ding, J.; Wang, H.; Cui, K.; Stephenson, T.; Karpuzov, D.; Mitlin, D. High Rate $SnO_2$−Graphene Dual Aerogel Anodes and Their Kinetics of Lithiation and Sodiation. *Nano Energy* **2015**, *15*, 369−378.

(26) Lu, Y. C.; Ma, C.; Alvarado, J.; Kidera, T.; Dimov, N.; Meng, Y. S.; Okada, S. Electrochemical Properties of Tin Oxide Anodes for Sodium-Ion Batteries. *J. Power Sources* **2015**, *284*, 287−295.

(27) Gu, M.; Kushima, A.; Shao, Y.; Zhang, J.-G.; Liu, J.; Browning, N. D.; Li, J.; Wang, C. Probing the Failure Mechanism of $SnO_2$ Nanowires for Sodium-Ion Batteries. *Nano Lett.* **2013**, *13*, 5203−5211.

(28) Wang, Y.; Su, D.; Wang, C.; Wang, G. $SnO_2$@MWCNT Nanocomposite as a High Capacity Anode Material for Sodium-Ion Batteries. *Electrochem. Commun.* **2013**, *29*, 8−11.

(29) Mullin, J. W. *Crystallization*, 3rd ed., Butterworth-Heinemann, London, 1997; DOI: 10.1002/cite.330701126.

(30) Bresser, D.; Mueller, F.; Buchholz, D.; Paillard, E.; Passerini, S. Embedding Tin Nanoparticles in Micron-Sized Disordered Carbon for Lithium- and Sodium-Ion Anodes. *Electrochim. Acta* **2014**, *128*, 163−171.

(31) Pires, F. I.; Joanni, E.; Savu, R.; Zaghete, M. A.; Longo, E.; Varela, J. A. Microwave-Assisted Hydrothermal Synthesis of Nanocrystalline SnO Powders. *Mater. Lett.* **2008**, *62*, 239−242.

(32) Sing, K. S. W. Reporting Physisorption Data for Gas/Solid Systems with Special Reference to the Determination of Surface Area and Porosity (Recommendations 1984). *Pure Appl. Chem.* **1985**, *57*, 603−619.

(33) Su, D.; Wang, C.; Ahn, H.; Wang, G. Octahedral Tin Dioxide Nanocrystals as High Capacity Anode Materials for Na-Ion Batteries. *Phys. Chem. Chem. Phys.* **2013**, *15*, 12543−12550.

(34) Courtney, I. A.; Dahn, J. R. Electrochemical and In Situ X-Ray Diffraction Studies of the Reaction of Lithium with Tin Oxide Composites. *J. Electrochem. Soc.* **1997**, *144*, 2045−2052.

(35) Liu, R.; Li, N.; Li, D.; Xia, G.; Zhu, Y.; Yu, S.; Wang, C. Template-Free Synthesis of $SnO_2$ Hollow Microspheres as Anode Material for Lithium-Ion Battery. *Mater. Lett.* **2012**, *73*, 1−3.

(36) Wang, J. W.; Liu, X. H.; Mao, S. X.; Huang, J. Y. Microstructural Evolution of Tin Nanoparticles During in Situ Sodium Insertion and Extraction. *Nano Lett.* **2012**, *12*, 5897−5902.

(37) Baggetto, L.; Ganesh, P.; Meisner, R. P.; Unocic, R. R.; Jumas, J.-C.; Bridges, C. A.; Veith, G. M. Characterization of Sodium Ion Electrochemical Reaction with Tin Anodes: Experiment and Theory. *J. Power Sources* **2013**, *234*, 48−59.

(38) Webb, S. A.; Baggetto, L.; Bridges, C. A.; Veith, G. M. The Electrochemical Reactions of Pure Indium with Li and Na: Anomalous Electrolyte Decomposition, Benefits of FEC Additive, Phase Transitions and Electrode Performance. *J. Power Sources* **2014**, *248*, 1105−1117.

(39) Dai, K.; Zhao, H.; Wang, Z.; Song, X.; Battaglia, V.; Liu, G. Toward High Specific Capacity and High Cycling Stability of Pure Tin Nanoparticles with Conductive Polymer Binder for Sodium Ion Batteries. *J. Power Sources* **2014**, *263*, 276−279.

(40) Li, S.; Wang, Y.; Qiu, J.; Ling, M.; Wang, H.; Martens, W.; Zhang, S. $SnO_2$ Decorated Graphene Nanocomposite Anode Materials Prepared Via an up-Scalable Wet-Mechanochemical Process for Sodium Ion Batteries. *RSC Adv.* **2014**, *4*, 50148−50152.

(41) Ji, L.; Gu, M.; Shao, Y.; Li, X.; Engelhard, M. H.; Arey, B. W.; Wang, W.; Nie, Z.; Xiao, J.; Wang, C.; Zhang, J.-G.; Liu, J. Controlling SEI Formation on SnSb-Porous Carbon Nanofibers for Improved Na Ion Storage. *Adv. Mater.* **2014**, *26*, 2901−2908.